Chapter 7

Optically induced transparency and tunable Fano resonance in micro-cavities

7.1 Introduction

Electromagnetically induced transparency and absorption (EMIT and EMIA) are the phenomena which give direct illustration of quantum interference effects. Quantum interference occurs due to interaction between pump laser field and driven atom. EMIT realized in atomic vapours [219, 220] followed by solid systems [221, 222]. In recent past, it was also observed in metamaterials [223], nano-mechanical mirror cavity [224], hybrid BEC optomechanics [225], micro-cavities [226], molecular magnetic system [227] etc. These have useful applications in information processing [228], storage of light [229], dark-state polaritons [230] and slow light [231]. Slow light has advantages in quantum and optical network [232], quantum memory [233]. The similar phenomena is also observed in the dynamics of OMS which are termed as optomechanically induced transparency and absorption (OMIT and OMIA). These are theoretically described and experimentally demonstrated in different OMSs [234-238]. These have potential utility in charge measurements [239], wavelength conversion [240], single photon router [241], ultra-slow light [235] and so on. Zhang et al have demonstrated PIT (Plasmon induced transparency) via Plasmon resonance [223]. Experimental work of CRIT (couple resonator induced transparency) for coupled micro-sphere system was performed by Totsuka et al [242]. Inverted-CRIT (ICRIT) was experimentally established in coupled ring resonator by Oishi and Tomita [243].

So, different optical cavity systems such as micro-spheres, micro-disks, micro-cavities, micro-rings and micro-resonators provide an attractive platform to study the above phenomena. The attention of the researchers has been fascinated by such systems due to high Q-factor and compact in size – which are relevant for device applications. In this chapter, we have analyzed the optically induced transparency (OIT) in coupled micro-

cavity system with tuneable tunnelling rate and balanced gain-loss. OIT has recently been discussed in the systems such as in bosonic lasers [244] and four-wave-mixing [245].

An interesting optical effect, called as Fano resonance, was first observed by Ugo Fano, in 1961 [246]. The Fano effect shows asymmetric sharp-line-shape profile. The occurrence of it is mainly due to quantum coherence and interference effect. Initially it has been described quantum mechanically but its classical analogy was illustrated by C. Alzar et al [247]. The existence of the line-shape nature has been already reported in distinct topics such as in hybrid OMS [248-250], PT-symmetry system [251], nano-particles [252], quantum well [253, 254], metamaterials [255], lossy multilayer surface and waveguide systems [256] etc. The effect provides a good platform in the field of quantum engineering such as light confinement [252], optical isolation [251], lasing without inversion [257], bio-sensors [258] etc. In spite of the above, recently, Fano effect has also been experimentally observed in different cavity system. Chiba et al described Fano effect in a micro-spherical cavity [259]. Li et al demonstrated Fano resonance in single micro-resonator [260]. Here, we have addressed the possibility of the tunable line-shape Fano profile in micro-cavity system.

7.2 The Model

The model system has already been described in section 6.3, chapter 6. The external driving laser field is given by $a^{in}(t) = E_c \exp(-i\omega_c t) + E_p \exp(-i\omega_p t)$. The input field has two parts, an intense control field and weakened probe field with frequencies ω_c , ω_p with field strengths E_c , E_p respectively ($E_c \gg E_p$).

The total Hamiltonian of the system is given by

$$H = \left(\omega_a - \frac{ik_a}{2}\right) a^\dagger a + \left(\omega_b - \frac{ik_b}{2}\right) b^\dagger b + J(ab^\dagger + a^\dagger b) + U a^{\dagger 2} a^2 + i\Omega_c\left(a^\dagger e^{-i\omega_c t} - a e^{i\omega_c t}\right) + i\Omega_p\left(a^\dagger e^{-i\omega_p t} - a e^{i\omega_p t}\right) \quad (7.1)$$

The field amplitudes are expressed by $\Omega_c = \sqrt{\eta k_a} E_c = \sqrt{\eta k_a P_c/\hbar\omega_c}$ and $\Omega_p = \sqrt{\eta k_a} E_p = \sqrt{\eta k_a P_p/\hbar\omega_p}$, where η indicates degree of the cavity coupling (cavity loading), P_c and P_p define the powers of the control and probe field, respectively. The loss rate k_a is sum of intrinsic and extrinsic cavity loss rate ($k_a = k_i + k_e$). The effective quality factor Q is related to k_a via relation $= \omega_a/k_a$. Alternatively, Q depends on intrinsic factor ($Q_i = \omega_a/k_i$) and coupling factor ($Q_e = \omega_a/k_e$). Different experimental works [261-263] reported that the Q factor can be changed by controlling different parameters. The cavity loading factor $\eta = k_e/k_a$, depends on k_i, k_e and Q. Experimental study reveals that η can be tuned by adjusting the gap between tapered fibre and micro-cavity setup [234]. This confirms that η have three possible regimes: $\eta < 1/2$ – under-coupling, $\eta = 1/2$ - critical-coupling and $\eta > 1/2$ - over-coupling regime, accordingly. In present analysis, we have studied OIT in two regimes – critical-coupling and over-coupling.

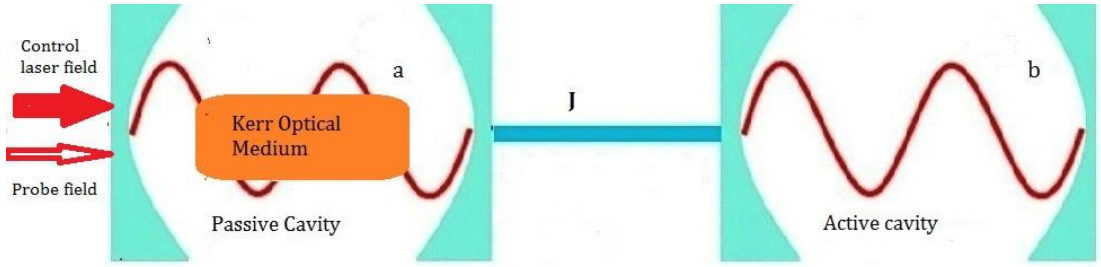

Figure 7.1: Schematic depiction of the model system with two coupled micro-cavities (passive and active). Passive cavity is driven by a weak probe field and a strong control field.

The system parameters used here are theoretically reported and experimentally established in different analysis. We have already been discussed those in chapter 5, section 5.2. In addition with this, as the system is driven by two input fields: a tunable external laser having 1450nm band is used as control or pump field and 1550nm as probe laser.

7.3 Quantum Dynamics

Reconstructing the system Hamiltonian (equation 7.1) under RWA at the control field frequency ω_c by means of $U(t) = \exp\{-i\omega_c(a^\dagger a + b^\dagger b)t\}$. We obtain the transformed Hamiltonian as

$$H' = \left(\Delta_a - \frac{ik_a}{2}\right)a^\dagger a + \left(\Delta_b - \frac{ik_b}{2}\right)b^\dagger b + J(a^\dagger b + ab^\dagger) + Ua^{\dagger 2}a^2 + i\Omega_c(a^\dagger - a) + i\Omega_p\left(a^\dagger e^{-i\Delta_p t} - ae^{i\Delta_p t}\right) \quad (7.2)$$

The detuning of cavity-control and probe-control fields are $\Delta_j = \omega_c - \omega_j$ $(j \in a, b)$ and $\Delta_p = \omega_p - \omega_c$, respectively. In presence of the quantum noise, the HLEs for the passive and active cavity modes are

$$\dot{a} = -\left(i\Delta_a + \frac{k_a}{2}\right)a - iJb - 2iUa^\dagger a^2 + \Omega_c + \Omega_p e^{-i\Delta_p t} + \sqrt{2k_a}a^{in}$$
$$\dot{b} = -\left(i\Delta_b + \frac{k_b}{2}\right)b - iJa + \sqrt{2k_b}b^{in} \quad (7.3)$$

The quantum noise operators a^{in} and b^{in} are obey following correlations

$$\langle a^{in}(t)a^{\dagger in}(t')\rangle = \langle b^{in}(t)b^{\dagger in}(t')\rangle = \delta(t - t')$$
$$\langle a^{\dagger in}(t)a^{in}(t')\rangle = \langle b^{\dagger in}(t)b^{in}(t')\rangle = 0 \quad (7.4)$$

As the probe field is very weaker than control field, so we can apply perturbation method. The control optical field supplies a steady state solution and weaker probe field

treated as noise. So, we can substitute the field operators as $a = a_s + \delta a$, $b = b_s + \delta b$ i.e. steady state value plus small fluctuation around it.

Neglecting fluctuation components, the steady state solutions can be obtained from following coupled equations

$$-\left(i\Delta_a + \frac{k_a}{2}\right) a_s - iJb_s - 2iU|a_s|^2 a_s + \Omega_c = 0$$

$$-\left(i\Delta_b + \frac{k_b}{2}\right) b_s - iJa_s = 0 \tag{7.5}$$

Again, considering the perturbation of weak probe field, we obtain

$$\frac{d}{dt}(\delta a) = G_1 \delta a - iJ\delta b + \Omega_p e^{-i\Delta_p t} + \sqrt{2k_a}a^{in}$$

$$\frac{d}{dt}(\delta b) = G_2 \delta b - iJ\delta a + \sqrt{2k_b}b^{in} \tag{7.6}$$

where $G_1 = \left(-i\Delta_a - \frac{k_a}{2} - 4iU|a_s|^2\right)$ and $G_2 = -\left(i\Delta_b + \frac{k_b}{2}\right)$, respectively.

Assuming the expectation of each operator of equation (7.6), we obtain (according to Markovian consideration, input noise operators have zero mean values)

$$\frac{d}{dt}(\langle\delta a\rangle) = F_1\langle\delta a\rangle - iJ\langle\delta b\rangle + \Omega_p e^{-i\Delta_p t}$$

$$\frac{d}{dt}(\langle\delta b\rangle) = F_2\langle\delta b\rangle - iJ\langle\delta a\rangle \tag{7.7}$$

The coupled field mode equations (7.7) are solved by using the following ansatz of the passive and active field fluctuation components

$$\begin{pmatrix}\langle\delta a\rangle \\ \langle\delta b\rangle\end{pmatrix} = \begin{pmatrix}A_- \\ B_-\end{pmatrix} e^{-i\Delta_p t} + \begin{pmatrix}A_+ \\ B_+\end{pmatrix} e^{i\Delta_p t} \tag{7.8}$$

From equation (7.7) and using (7.8), after tedious algebraic calculations, we derive following expressions (detailed in appendix D)

$$A_- = \frac{-\Omega_p(G_2 + i\Delta_p)}{J^2 - {\Delta_p}^2 + G_1G_2 + i\Delta_p(G_1 + G_2)}$$

$$B_- = \frac{-J\Omega_p}{J^2 - {\Delta_p}^2 + G_1G_2 + i\Delta_p(G_1 + G_2)} \tag{7.9}$$

Applying standard input-output formalism

$$a_{out} = a_{in} - \sqrt{\eta k_a}a(t) \text{ and } b_{out} = -\sqrt{\eta k_b}b(t) \tag{7.10}$$

The output field modes at the forward transmission and backward reflection are given by

$$a_{out} = \frac{1}{\sqrt{\eta k_a}}\left[(\Omega_c - \eta k_a a_s)e^{-i\omega_c t} + \left(\Omega_p - \eta k_a A_-\right)e^{-i\omega_p t} - \eta k_a A_+ e^{-i(2\omega_c - \omega_p)t}\right]$$

$$b_{out} = \sqrt{\eta k_b}\left[-b_s e^{-i\omega_c t} - B_- e^{-i\omega_p t} - B_+ e^{-i(2\omega_c - \omega_p)t}\right] \tag{7.11}$$

From the equation (7.10), it is easily observed that output fields contain three frequencies. First, two frequencies are related to the control field and the probe field. Third one is an accompanying frequency component $(2\omega_c - \omega_p)$, related to Stokes field [264]. To illustrate forward transmission and backward reflection profiles, we focus on the probe field component.

The ratios of the output field to the input field amplitude for transmission along forward direction and reflection along backward direction are given by

$$t(\omega_p) = 1 - \frac{\eta k_a A_-}{\Omega_p} \text{ and } r(\omega_p) = \frac{\sqrt{k_a k_b}\,\eta\, B_-}{\Omega_p} \tag{7.12}$$

The forward transmission rate (FTR) $T_F = \left|t(\omega_p)\right|^2$ and backward reflection rate (BRR) $T_B = \left|r(\omega_p)\right|^2$ of the probe field are expressed as follows:

$$T_F = \left|1 - \frac{\eta k_a F_1(\Delta_p)}{F_2(\Delta_p) + F_3(\Delta_p)}\right|^2 \tag{7.13}$$

$$T_B = \left|\frac{\eta J\sqrt{k_a k_b}}{F_2(\Delta_p) + F_3(\Delta_p)}\right|^2 \tag{7.14}$$

Where $F_1(\Delta_p) = i(\Delta_b - \Delta_p) + \frac{k_b}{2}$, $F_2(\Delta_p) = J^2 - {\Delta_p}^2 - \Delta_a\Delta_b + \Delta_a\Delta_p + \Delta_b\Delta_p - 4U|a_s|^2(\Delta_b - \Delta_p) - \frac{k_a k_b}{4}$ and $F_3(\Delta_p) = \frac{i}{2}\{k_a(\Delta_b - \Delta_p) + k_b(\Delta_a - \Delta_p)\}$.

Using expressions of equation (7.13) and (7.14), we have analyzed the variation of forward transmission profile (FTP) and backward reflection profile (BRP) as a function of different system parameters, are described in next sections.

7.4 Forward transmission and backward reflection spectra

We have illustrated the FTP and BRP at critical cavity loading i.e. for $\eta = 1/2$. In Figure 7.2(a-d), we present how the FTR (T_F) and BRR (T_B) explicitly depend on the probe detuning for different tunnelling rate (J) and gain-to-loss ratio (k_b/k_a). From figure 7.2a, it is clear that FTP shows a single transparent peak about zero probe detuning i.e. $\Delta_p/k_a = 0$ with two dips (super modes) on both side. The profile shows symmetric dip-peak-dip pattern and it signify OIT effect in present system. Figure 7.2b, displays the variation for higher photon tunnelling rate i.e. for $J/k_a = 1$. The dips are at $\Delta_p/k_a = -1$ and $\Delta_p/k_a = +1$, respectively. The wideness of the transparency windows is $2J$. By adjusting separation between the micro-cavities i.e. controlling tunnelling rate one may tune the width of the OIT window. The generation of OIT window is stated as follows: destructive interference between the probe and the side-band field causes to dropping of the intra-cavity field. For both the cases, the value of T_B is very small as the ratio k_b/k_a is small. Figure 7.2 (c-d) depict same variation with higher k_b/k_a. Interestingly, the value of T_B is considerably enhanced as k_b/k_a ratio is increased. So, reflection rate can be controlled by adjusting the value of k_b/k_a i.e. controlling the system interaction with the environment in which system embedded. Here, width of the transmission profile remains same but the peak values decreases.

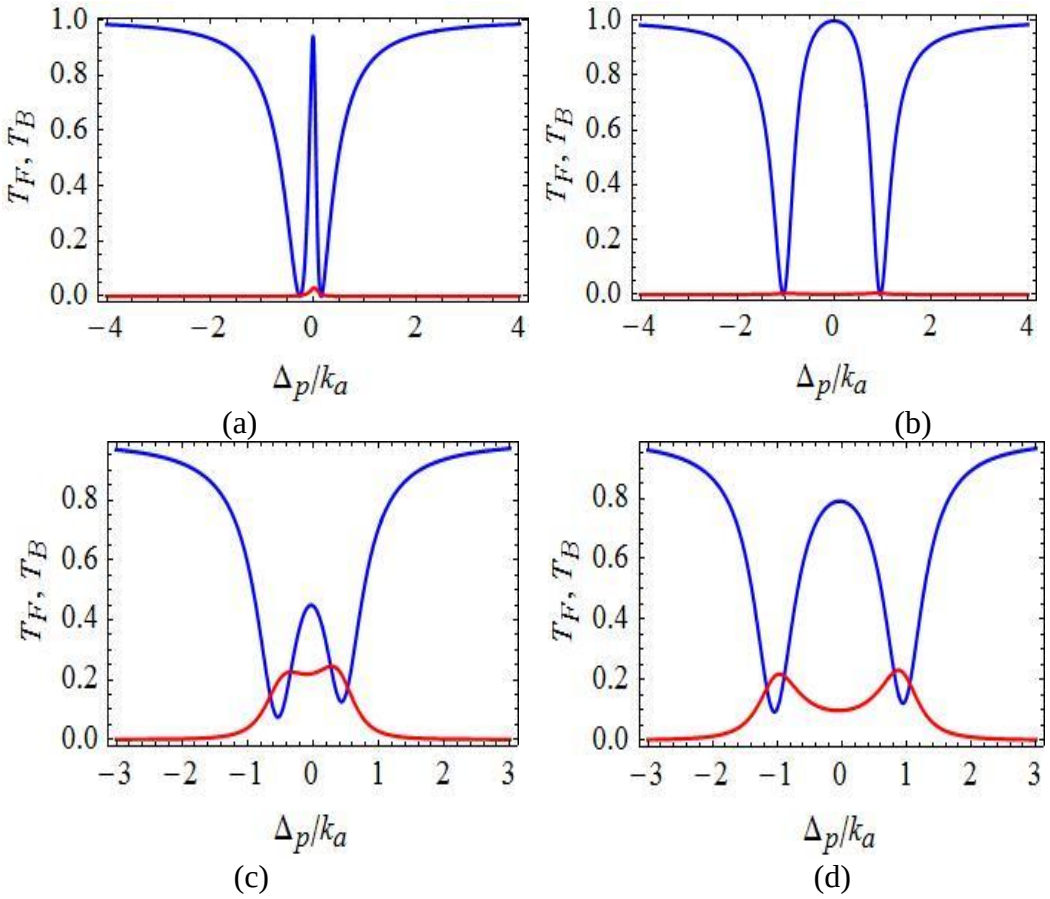

Figure 7.2: Variation of forward transmission rate T_F (blue line) and backward reflection rate T_B (red line) with normalised probe detuning Δ_p/k_a for $\Delta_a/k_a = -0.1$, $\Delta_b/k_a = 0.0$, $U/k_a = 0.01$, $|a_s| = 0.06$ (a) $k_b/k_a = 0.005$, $J/k_a = 0.2$ (b) $k_b/k_a = 0.005$, $J/k_a = 1.0$ (c) $k_b/k_a = 0.5$, $J/k_a = 0.5$ and (d) $k_b/k_a = 0.5$, $J/k_a = 1.0$.

Now, we describe the FTP and the BRP at over cavity loading regime $(\eta = 2)$ i.e. for $\eta > 1/2$. Figure 7.3 (a-d) depict the dependence of T_F and T_B on probe detuning for PPCS with $k_b/k_a = 0.0001, k_b/k_a = 0.001, k_b/k_a = 0.01$ and $k_b/k_a = 0.05$. The FTP conveys a dip around zero probe frequency detuning which gives the signature of the forward transmission of the probe beam and shows the generation of the OIT. From these graphical representations, it is clear that probe transmission increases with k_b/k_a and complete transmission is possible for $k_b/k_a = 0.001$ (figure 7.3b). This is due to

destructive interference between the anti-stokes and the probe field. If k_b/k_a ratio further increases then the rate of the transmission decreases gradually (figure 7.3c and 7.3d). The variation of the T_B shows that reflection rate increases as the ratio of k_b/k_a raises (figure 7.3c). This enhancement is due to the higher k_b/k_a ratio (similar variation of T_B is obtained for critical cavity loading). The T_B peak is due to constructive interference. For $k_b/k_a = 0.05$, the reflection rate T_B decreases and width of the profile is broaden.

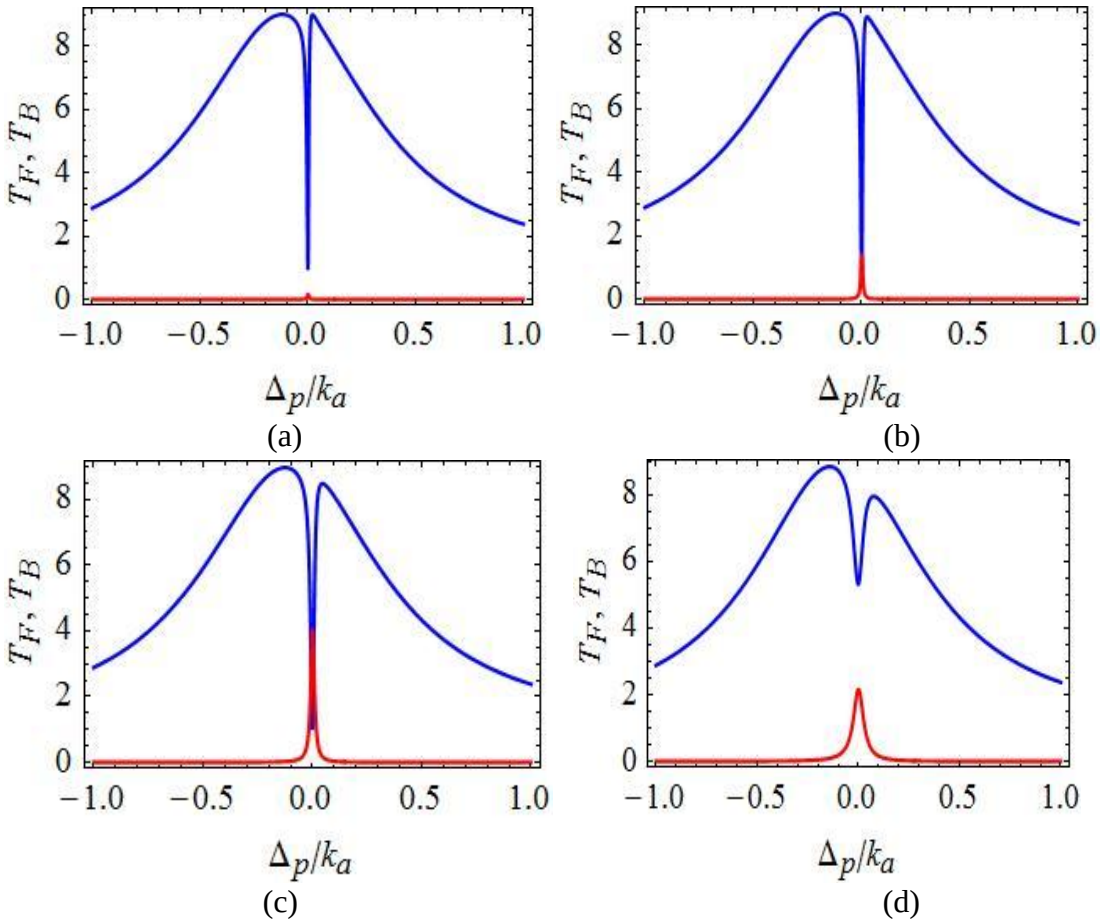

Figure 7.3: Variation of forward transmission rate T_F (blue line) and backward reflection rate T_B (red line) with normalised probe detuning Δ_p/k_a for $\Delta_a/k_a = 0.1$, $\Delta_b/k_a = 0.0, U/k_a = 0.01, |a_s| = 0.06,\ J/k_a = 0.05$ (a) $k_b/k_a = 0.0001$ (b) $k_b/k_a = 0.001$ (c)$k_b/k_a = 0.01$ (d)$k_b/k_a = 0.05$.

Figure 7.4 (a-d) present the variation of T_F and T_B with different tunnelling rate at over cavity loading. The profiles of T_F show a dip whereas T_B show a sharp peak about $\Delta_p/k_a = 0$. For normalised tunnelling rate $J/k_a = 0.005$ the dip intensity of T_F and peak intensity of T_B both are very feeble (figure 7.4a).

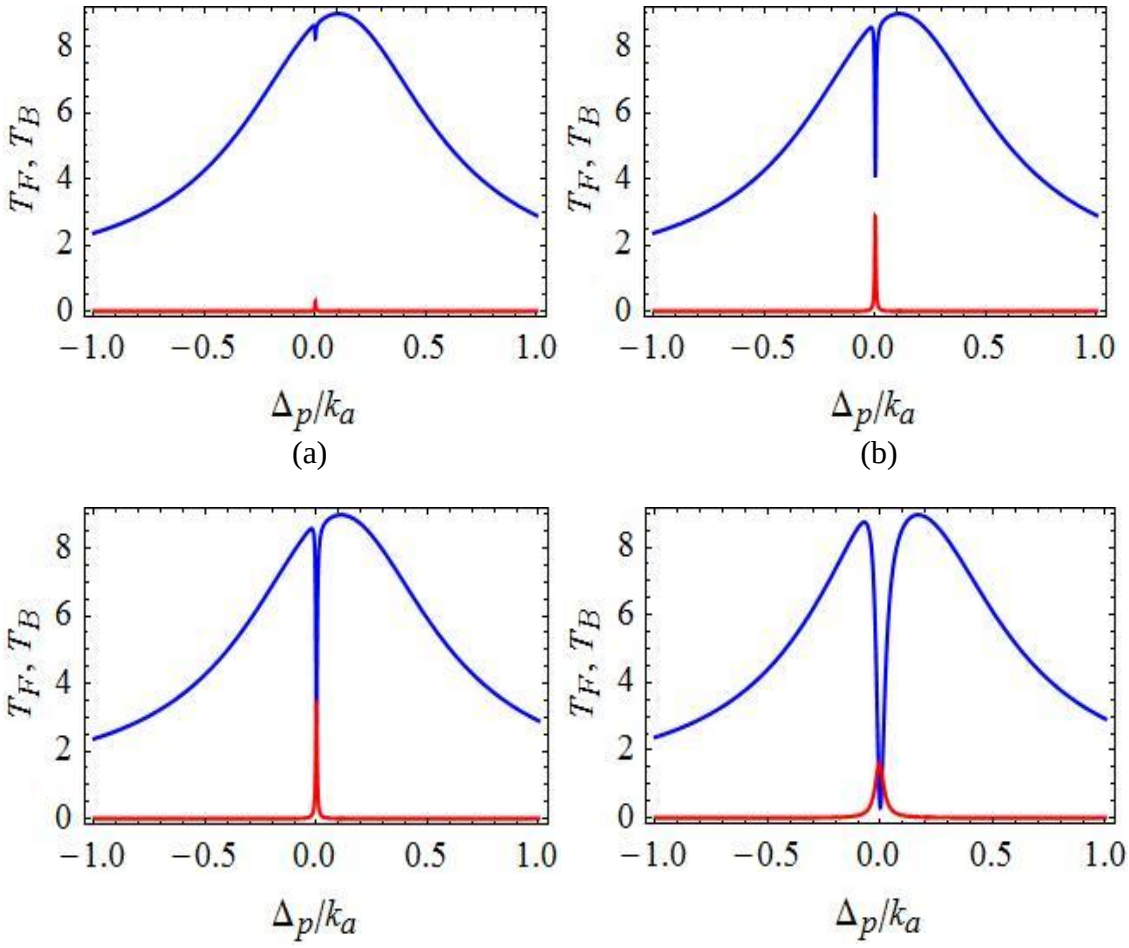

Figure 7.4: Variation of forward transmission rate T_F (blue line) and backward reflection rate T_B (red line) with normalised probe detuning Δ_p/k_a for $k_b/k_a = 0.005, U/k_a = 0.01$, $\Delta_a/k_a = -0.1$, $\Delta_b/k_a = 0.0$, $|a_s| = 0.06$ (a) $J/k_a = 0.005$ (b) $J/k_a = 0.02$ (c) $J/k_a = 0.025$ and (d) $J/k_a = 0.1$.

The dip intensity significantly enhanced as the value of J increases. When J increases from $0.005k_a$ to $0.02k_a$ (figure 7.4b) and $0.025k_a$(figure 7.4c) the dip intensity of T_F is more deeper and peak intensity of T_B is significantly enriched. For $J = 0.1k_a$, the

dip intensity reaches optimum value that indicates complete transmission of the probe field (Figure 7.4d). The peak height of T_B decreases but the width increases. Further increasing of the tunnelling rate, both the dip and peak intensity lowers.

7.5 Asymmetric Fano line shape

In previous section, we discussed about the FTP and BRP at critical and over loading regime for PPCS. Here, we focus on the transmission profiles at both regime but for PACS. At first, we interpret the profiles at critical cavity loading and the results are plotted in figure 7.5 (a-d).

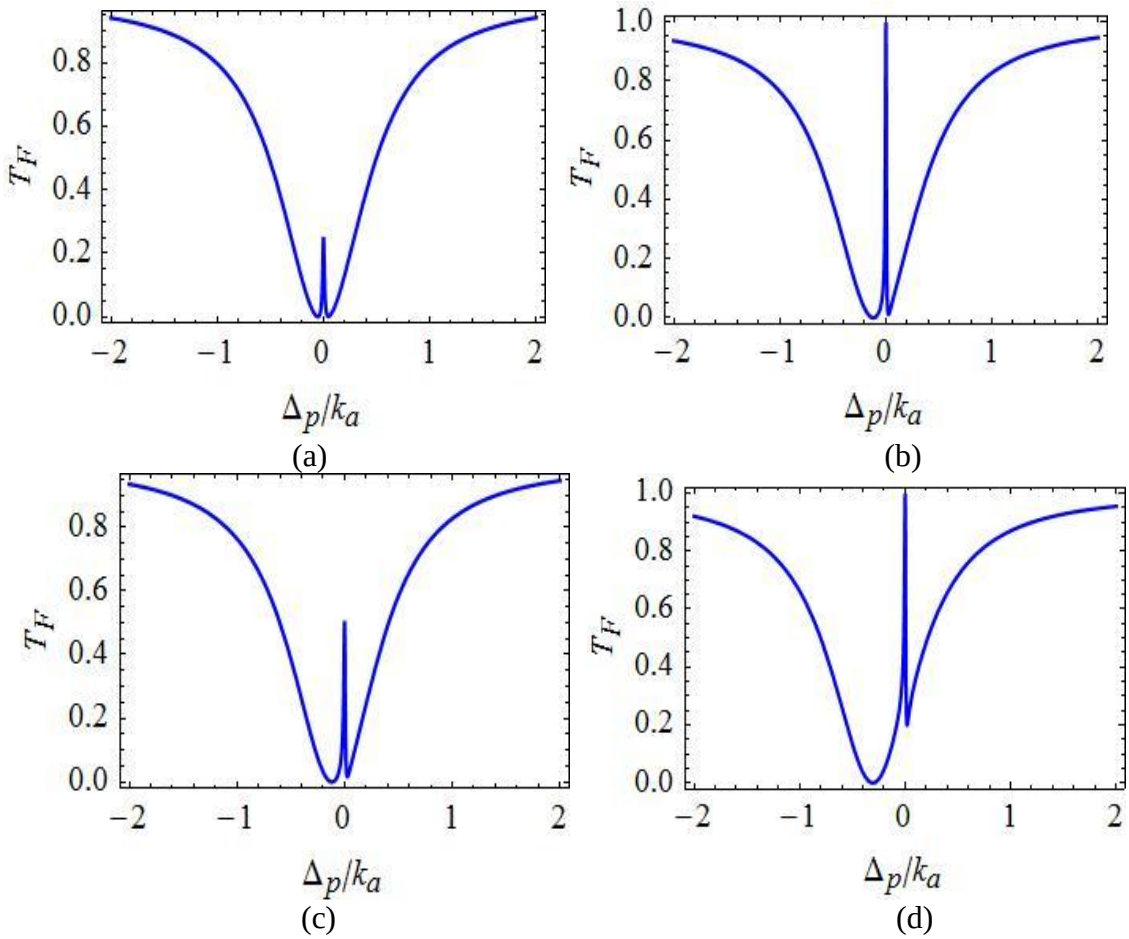

Figure 7.5: Forward transmission rate T_F as a function of probe detuning Δ_p/k_a for $U/k_a = 0.01$, $\Delta_b/k_a = 0, J/k_a = 0.05, |a_s| = 0.06$(a) $k_b/k_a = -0.03$, $\Delta_a/k_a = -0.01$ (b) $k_b/k_a = -0.02$, $\Delta_a/k_a = -0.1$ (c) $k_b/k_a = -0.025$, $\Delta_a/k_a = -0.1$ and (d) $k_b/k_a = -0.02$, $\Delta_a/k_a = -0.3$.

The transmission spectra shows line-shape profile around zero probe detuning. Figure 7.5a depicts the variation for passive cavity frequency detuning $\Delta_a = -0.01k_a$. The FTP shows a sharp transparent peak at $\Delta_p = 0$ and two symmetric dips both side of it. If detuning changes from $\Delta_a = -0.01k_a$ to $\Delta_a = -0.1k_a$, the profile shows asymmetric in nature with higher peak intensity (figure 7.5b). Keeping same detuning, the effective gain is changed to $k_b = -0.025k_a$, the peak intensity of the line shape lowered (figure 7.5c). The peak totally disappears for $k_b = -0.1k_a$. So, the FTP may be tuned by controlling gain-to-loss (k_b/k_a) ratio. For $\Delta_a = -0.3k_a$, the transmission profile is highly asymmetric (figure 7.5d). The asymmetric (figure 7.5b-7.5d) line shape profile is due to Fano resonance. On approaching to the zero probe detuning from right, the transition from dip to peak occurs very abruptly while approaching from left, the transition from dip to peak comparatively slows down.

Now, we have described the dependence of T_F on probe detuning with different ratio of k_b/k_a for PACS. Figure 7.6 (a-c) depict the variation with the gain-loss ratio $k_b/k_a = -0.004$, $k_b/k_a = -0.003$ and $k_b/k_a = -0.0025$, respectively. Figure 7.6a shows an absorptive nature of the probe field. When the ratio of k_b/k_a is changed from -0.004 to -0.003 , a significant change (line-shape) in nature of FTP is observed. Figure 7.6(b-d) represent the sharp line structure i.e. signature of the asymmetric Fano line-shape. The Fano line-shape profile is generated due to presence of the interaction term or passive-active mode coupling part $(ab^{\dagger} + a^{\dagger}b)$, in the system Hamiltonian. Due to this term, back and forth reflection of the cavity fields through distinct pathways causes destructive interference. From figure 7.6(b-c), it is clear that asymmetric line-shape structure may be tuned by adjusting gain-to-loss (k_b/k_a) ratio. The optimum asymmetric Fano like transition is observed for $k_b/k_a = -0.003$ (Figure 7.6 b). An

analysis of figure 7.6b leads to following observations: This Fano line has resonance dip at $\Delta_p = 0.00347k_a$ and peak at $\Delta_p = -0.00599k_a$. The Fano spectral broadening is $0.00946k_a$. The transmission contrast along the forward direction of the Fano profile is approximately 60%, which satisfies the optimum criterion of any Telecom system [265].

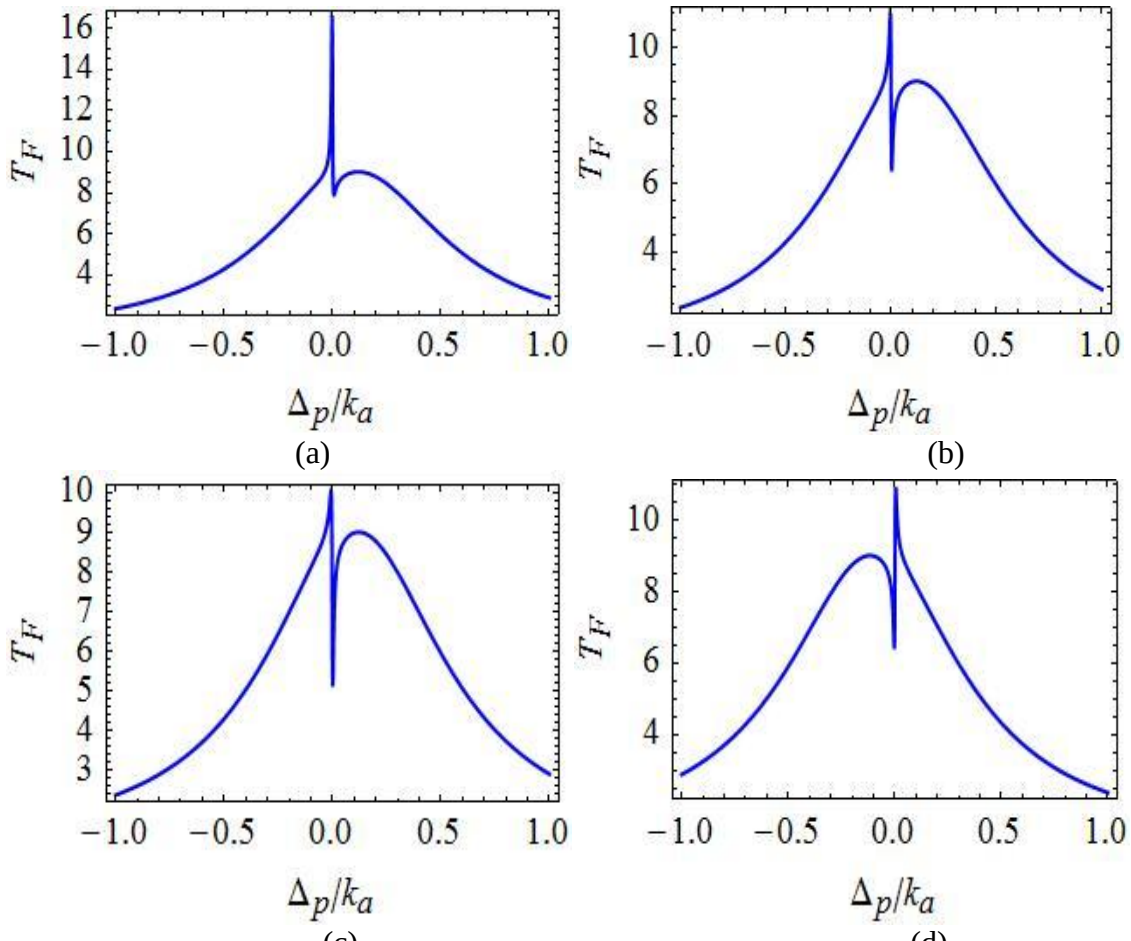

Figure 7.6: Forward transmission rate T_F as a function of probe detuning Δ_p/k_a for $U/k_a = 0.01$, $\Delta_b/k_a = 0.0$, $J/k_a = 0.05$, $|a_s| = 0.06$ (a) $k_b/k_a = -0.004$, $\Delta_a/k_a = 0.1$ b) $k_b/k_a = -0.003$, $\Delta_a/k_a = 0.1$ c) $k_b/k_a = -0.0025$, $\Delta_a/k_a = 0.1$ d) $k_b/k_a = -0.003$, $\Delta_a/k_a = -0.1$.

The present analysis also reveals that the Fano response also changes significantly with tunnelling rate and slightly with Kerr nonlinearity. When the tunnelling rate increases

from $0.05k_a$ to $0.07k_a$, the dip of the Fano response decreases considerably (very close to zero) and beyond that the response is signed out. If the value of J lower from $0.05k_a$ to $0.04k_a$, the line shape just emerges out. At $J = 0.01k_a$, the response shows a sharp peak (similar to figure 7.6a) – this implies absorptive in nature. Again, when the nonlinear strength lowers from $U = 0.01k_a$ to $0.001k_a$, the FTP shows almost same variation but sharpness of the Fano resonance is slightly enriched. At $U = 0.08k_a$, the Fano line-response is ruled out and FTP shows absorptive in nature. Figure 7.6d is just mirror image of figure 7.6b. Here passive cavity detuning varies from $\Delta_a = 0.1k_a$ to $\Delta_a = -0.1k_a$, other parameters are same.

7.6 Summary

We have analyzed OIT and asymmetric Fano resonance in coupled micro-cavities. One is passive and other is active micro-cavity. The cavities are coupled via photon tunnelling. The passive micro-cavity is externally driven by two-tone laser – control and probe field. We have illustrated an analytical model to solve coupled HLEs by using perturbation method and input-output formalism and obtained the expressions of FTR and BRR. The variations of both the forward transmission and backward reflection profiles of the weak probe field are studied at critical and over cavity loading regime for PACS and PPCS. Our approach is somewhat different from the method followed in reference [49].

At critical loading degree, the FTP of the PPCS shows dip-peak-dip spectral pattern. The pattern is symmetric about zero probe field frequency detuning. As tunnelling rate increases the separation between the dip increases and a transparency window is formed. The width of the window may be tuned by adjusting tunnelling rate between the two micro-cavities. The formation of the window is due to destructive interference

between the probe and side-band fields. Again, BRR is very small for lower values of k_b/k_a . The reflection rate (T_B) enhanced as tunnelling rate and k_b/k_a ratio increases.

For PACS the transmission profiles symmetric and shows a transparent peak at $\Delta_p = 0$ and two dip both-sides of it, for passive cavity detuning $\Delta_a = -0.01k_a$. The profile is asymmetric when the negative values of Δ_a increases. The peak intensity depends on the ratio of k_b/k_a. This asymmetric line structure of FTP is related to Fano resonance.

At over cavity loading regime, the FTP shows a dip and BRP shows a peak about $\Delta_p = 0$ for PPCS. The dip intensity and peak height depend on tunnelling rate and ratio of k_b/k_a (both have an upper limit as discussed in section 7.4). Variation of BRR is similar to critical loading. But intensity of BRR is larger at over loading as compared to critical cavity loading.

For PACS the FTP shows sharp asymmetric line-shape which implies the occurrence of the Fano resonance. The origin of the Fano response may be explained from passive-active field mode coupling part of the model Hamiltonian. Due to this term the back and forth reflections of the optical field between distinct pathways occur and hence resulting quantum interference. The sharpness, spectral broadening and asymmetric behaviour of the Fano profile can be tuned via passive cavity detuning, tunnelling rate, gain-to-loss rate and Kerr strength. Our study may be useful for modelling sensitive sensor. In present analysis, the contrast of the Fano profile is so intense which satisfy essential criterion for any Telecom system.